Chemical Geology 625 (2023) 121432

Contents lists available at ScienceDirect

Chemical Geology

journal homepage: www.elsevier.com/locate/chemgeo

Re-evaluation of equilibrium relationships involving U^{6+}/U^{4+} and Fe^{3+}/Fe^{2+} in hydrothermal fluids and their implications for U mineralization

Teng Deng [a,b,c], Guoxiang Chi [d,**], Anthony E. Williams-Jones [e], Zenghua Li [a,b,c,*], Yumeng Wang [d], Deru Xu [a,b,c], Zhilin Wang [f]

[a] Fundamental Science on Radioactive Geology and Exploration Technology Laboratory, East China University of Technology, Nanchang 330013, China
[b] State Key Laboratory of Nuclear Resources and Environment, East China University of Technology, Nanchang 330013, China
[c] School of Earth Sciences, East China University of Technology, Nanchang 330013, China
[d] Department of Geology, University of Regina, Regina S4S 0A2, Canada
[e] Department of Earth and Planetary Sciences, McGill University, Quebec H3A 2A7, Canada
[f] Key Laboratory of Metallogenic Prediction of Nonferrous Metals and Geological Environment Monitoring, Ministry of Education, School of Geosciences and Info-Physics, Central South University, Changsha 410083, China

ARTICLE INFO

Editor: Hailiang Dong

Keywords:
Uranium transport
Uranium precipitation
Uranium solubility
Iron solubility
Redox
U-Fe co-transport
Hematization
Geochemical modeling

ABSTRACT

Uranium (U) and iron (Fe) are generally considered to have contrasting aqueous geochemical behavior, with U dissolution being favored in oxidizing fluids as oxidized U (U^{6+}) and Fe in reducing fluids as reduced Fe (Fe^{2+}) species. However, high concentrations of both U and Fe have been reported for the ore fluids of uranium deposits, suggesting that the two elements can be co-transported in the same fluid. In this study, geochemical modeling, based on recent thermodynamic and experimental data for U and Fe species and fluid inclusion compositions from two types of hydrothermal U deposits (volcanic-related and unconformity-related), was conducted to investigate the nature and conditions of U—Fe co-transportation. The results of the modeling indicate that high concentrations of U (>10, up to >100 ppm) and Fe (>1000 ppm) can be dissolved in acidic aqueous fluids (pH < ~3.3) of moderate to high chlorinity (~ 55 to 250 g/L Cl), for a wide range of logfO_2 above and below the magnetite-hematite (MH) buffer (from ~ MH-5 to MH + 30), at temperatures from 150 to 250 °C. There are four different combinations of dominant dissolved U and Fe species depending on the pH and redox conditions: U^{6+} and Fe^{3+} species ($UO_2Cl_2^0$ and $FeCl_3^0$) at relatively high fO_2, U^{4+} and Fe^{2+} species (UCl_4^0 and $FeCl_4^{2-}$) at relatively low fO_2, and U^{6+} and Fe^{2+} species ($UO_2Cl_2^0$ and $FeCl_4^{2-}$) or U^{4+} and Fe^{3+} species (UCl_4^0 and $FeCl_3^0$) at intermediate fO_2 conditions. Because the most important U mineral in hydrothermal uranium deposits is uraninite (UO_2), in which U is present as U^{4+}, a necessary condition for U mineralization is that U is either transported as U^{4+} species or, if transported as U^{6+} species, precipitation of uraninite is induced by a reducing agent. The recognition that U^{6+} and Fe^{2+} species can be co-transported in the same fluid indicates that uraninite can be precipitated without the need to invoke a reducing agent external to the ore fluid. The driver of uranium mineralization in this case is an increase in pH due to fluid-rock interaction that leads to the alteration of the rocks by clay minerals and associated coupled sorption-reduction. These findings provide for a more extensive range of conditions for U transport and deposition than previously imagined and require that interpretation of the conditions of uranium mineralization consider both oxygen fugacity and pH. This study underscores the potential for uranium deposits to occur in geological settings where reducing agents are either absent or insufficiently abundant to account for the observed mineralization, and the possibility for the transport of U in environments that might otherwise be considered unfavorable.

* Corresponding author at: Fundamental Science on Radioactive Geology and Exploration Technology Laboratory, East China University of Technology, Nanchang 330013, China.
** Corresponding author.
E-mail addresses: guoxiang.chi@uregina.ca (G. Chi), lizenghua@ecut.edu.cn (Z. Li).

https://doi.org/10.1016/j.chemgeo.2023.121432
Received 19 October 2022; Received in revised form 26 January 2023; Accepted 13 March 2023
Available online 15 March 2023
0009-2541/© 2023 Elsevier B.V. All rights reserved.

1. Introduction

Many geological observations and geochemical experiments have concluded that uranium (U) is much more soluble in the hexavalent (U^{6+}) than in the tetravalent form (U^{4+}) in geofluids at low (near surface) to moderate (~ 300 °C) temperature (Langmuir, 1978; Romberger, 1984; Mernagh et al., 1994; Wersin et al., 1994; Komninou and Sverjensky, 1996; Cuney, 2009; Bastrakov et al., 2010; Dargent et al., 2013, 2015; Cuney and Kyser, 2015; Cumberland et al., 2016; Xing et al., 2018, 2019). Based on this general understanding of the aqueous geochemistry of uranium, redox reactions that transform U^{6+} to U^{4+} have been considered to be a key factor controlling uranium mineralization in a variety of geologic environments (Romberger, 1984; Cuney and Kyser, 2015). Consequently, the identification of redox fronts, where oxidizing fluids carrying U^{6+} meet with rocks or fluids enriched in reducing agents, has been used as an important uranium exploration strategy (IAEA (International Atomic Energy Agency), 2018).

In some cases, however, the rocks hosting uranium deposits do not appear to contain a sufficient abundance of a suitable reducing agent to explain the observed uranium mineralization, and there is no unambiguous evidence for the involvement of a separate fluid carrying a reducing agent. Examples of such deposits are jasper-quartzite-hosted U (Volzhin and Korolev, 1982; Goswami et al., 2019) and leucogranite-hosted U (Liang et al., 2017). Because of the lack of evidence for a reducing agent for such uranium deposits, consideration has been given to the possibility that the required U could be transported as U^{4+} species, thereby avoiding the need for a reducing agent. Indeed, support for this possibility has been provided by a recent experimental study of U solubility, which showed that U can be dissolved in significant concentrations as U^{4+} species ($UCl^0_{4(aq)}$) in fluids of high chlorinity, under acidic and relatively reducing conditions at temperatures >100 °C (Timofeev et al., 2018). A fluid transporting U under such conditions would deposit uraninite or pitchblende in response to an increase in pH or a decrease in temperature without reduction. The same study also showed, however, that at relatively oxidizing conditions (oxygen fugacity greater than that of the magnetite-hematite (MH) buffer), the U^{6+} species ($UO_2Cl_{2(aq)}$) is considerably more important than $UCl^0_{4(aq)}$ (Timofeev et al., 2018). Thus, for deposits for which there is evidence that the ore fluid was oxidized (above the MH buffer), but there is no evidence for the required amount of reducing agent in the host rocks or for the mixing of the ore fluid with a fluid containing a suitable reducing species, an alternative solution to the problem of reduction must be sought. One potential solution is the transport of U^{6+} with reducing agents in the same fluid, and a redox reaction within the fluid triggered by a pH change due to fluid-rock interaction.

A recent experimental study by Dargent et al. (2015) suggests that, whereas many reducing species, e.g., CH_4 and H_2, spontaneously reduce U from U^{6+} to U^{4+} and therefore cannot be co-transported with U^{6+}, high concentrations of Fe^{2+} (0.1 mol/kg or 5600 ppm) can coexist without reaction with high concentrations of U^{6+} (10^{-3} mol/kg or 235 ppm) in acidic brines (pH ≈ 1) for protracted periods of time (> 18 days). Furthermore, high concentrations of Fe (100–10,000 ppm) and U (1–100 ppm, up to 600 ppm) have been reported in fluid inclusions from hydrothermal U deposits (Richard et al., 2012, 2016; Martz et al., 2019; Yu et al., 2019), suggesting that the elevated Fe and U solubility in the experiment of Dargent et al. (2015) may be an equilibrium rather than a kinetic phenomenon. Therefore, contrary to the commonly held belief that U and Fe have contrasting geochemical behavior, with U being more soluble in oxidizing fluids (as U^{6+} species) and Fe being more soluble in reducing fluids (as Fe^{2+} species), it is possible that U^{6+} and Fe^{2+} may dissolve in significant amounts in the same fluid. This possibility requires quantitative evaluation, using the best available data for the thermodynamic properties of oxidized and reduced U and Fe species, for the range of conditions interpreted for various types of uranium deposits.

During the past two decades great advances have been made in our understanding of the solubility and speciation of Fe and U in hydrothermal fluids (e.g., Liu et al., 2006, 2007; Soderholm et al., 2011; Dargent et al., 2013, 2015; Timofeev et al., 2018; Stefánsson et al., 2019). For example, a reassessment of the thermodynamic properties of Fe^{2+}-bearing chloride and hydroxy complexes have shown that the Fe^{2+} species are stable at fO_2 well above the MH buffer (e.g., log fO_2 < HM + 7.2 at pH = 3 and T = 250 °C) (Liu et al., 2006; Scholten et al., 2019; Gammons and Allin, 2022). This finding, taken in conjunction with reassessments of the thermodynamic properties of UO_2^{2+} chloride and hydroxy complexes (Dargent et al., 2013; Xing et al., 2018; Migdisov et al., 2019), provides strong support for the notion that U^{6+} and Fe^{2+} can be transported in the same hydrothermal fluid over a wide interval of physicochemical conditions.

In this contribution, we model the equilibrium dissolution of U and Fe in hydrothermal fluids containing a variety of ligands using Geochemist Workbench (GWB) (Bethke et al., 2018, 2020) and the database provided in the software plus newly published data on the thermodynamic properties of U- and Fe-bearing species. We use the geochemical data for fluid inclusions from two types of hydrothermal U deposits, the Zoujiashan volcanic-related U deposit in the Xiangshan ore field, South China (Yu et al., 2019) and the unconformity-related U deposits in the Athabasca Basin, Canada (Richard et al., 2012, 2016), to represent the ore fluid compositions. The purpose of the study is to provide an updated account of the solubility and speciation of U and Fe in hydrothermal solutions at different pH and redox conditions and at fluid compositions and thermal conditions relevant to many hydrothermal uranium deposits. In particular, we aim to determine whether or not, and under what conditions, U^{6+} and Fe^{2+} can be co-transported in hydrothermal fluids, and to examine the mechanism driving the redox reaction within the fluid that leads to uranium mineralization. Finally, the significance of the modeling results for uranium mineralization and exploration is examined.

2. Thermodynamic database and modeling method

The thermodynamic database used in this study was modified from the Lawrence Livermore National Laboratory database (the LLNL dataset, thermo.com.v8.r6+) that is provided in the Geochemist's Workbench® (GWB) software package (Bethke, 2007; Bethke et al., 2018, 2020). Thermodynamic properties and log K values of reactions involving a variety of U-bearing aqueous and mineral species for a series of temperatures (0, 25, 60, 100, 150, 200, 250, 300 °C) are provided in the default thermo.com.v8.r6+ database. These species comprise $(UO_2)_2(OH)_2^{2+}$, $(UO_2)_3(CO_3)_6^{6-}$, $(UO_2)_3(OH)_5^+$, $U(CO_3)_5^{6-}$, $U(OH)_{4(aq)}$, $U(SO_4)_{2(aq)}$, UCl^{3+}, UF^{3+}, UF_2^{2+}, UF_3^+, $UO_2(CO_3)_2^{2-}$, $UO_2(CO_3)_3^{4-}$, $UO_2(SO_4)_2^{2-}$, UO_2Cl^+, $UO_2ClO_3^+$, UO_2F^+, $UO_2F_3^-$, $UO_2F_4^{2-}$, UO_2OH^+, $UO_2SO_{4(aq)}$, UOH^{3+}, USO_4^{2+}, UO_2 (uraninite), U_3O_8, U_4O_9, $UO_4(OH)_2$(-beta), $Na_2U_2O_7$ and $CaUO_4$. New thermodynamic properties for U-bearing minerals and aqueous species were compiled and evaluated by Xing et al. (2018), namely U^{3+}, $(UO_2)_2(OH)_2^{2+}$, UO_2^+, UO_2^-, UOH^{2+}, U^{4+}, UO^+, UO^{2+}, UO_3^-, UO_4^{2-}, $UO_{3(aq)}$, $HUO_{2\ (aq)}$, HUO_3^-, HUO_4^-, $UO_{2\ (aq)}$, $U(OH)^{3+}$, HUO_2^+, $UO_2OH_{\ (aq)}$, UO_2OH^+, $(UO_2)_2(OH)_2^{2+}$, $(UO_2)_2(OH)_2^{3+}$, $(UO_2)_3(OH)_4^{2+}$, $(UO_2)_3(OH)_5^+$, $(UO_2)_3(OH)_7^-$, $(UO_2)_4(OH)_7^+$, UF^{3+}, UF_2^{2+}, UF_3^+, $UF_{4(aq)}$, UF_5^-, UF_6^{2-}, UO_2F^+, $UO_2F_{2\ (aq)}$, $UO_2F_3^-$, $UO_2F_4^{2-}$, UCl^{3+}, UCl_2^{2+}, $UO_2Cl_{(aq)}$, $UO_2Cl_2^-$, UO_2Cl^+, $UO_2Cl_{2(aq)}$, USO_4^{2+}, $U(SO_4)_{2(aq)}$, $UO_2SO_{4(aq)}$, $UO_2(SO_4)_2^{2-}$, $UO_2F_{2\ (cr)}$, coffinite, and $UO_{3(cr)}$. The thermodynamic properties of the newly recognized reduced aqueous species, $UCl_{4(aq)}$ (Timofeev et al., 2018), were extrapolated by Migdisov et al. (2019) from the data of Timofeev et al. (2018). All these data were imported into the Unitherm database of HCh (Shvarov and Bastrakov, 1999) to calculate the log K values of the relevant reactions, which were then incorporated into the GWB database for geochemical modeling. As carbonate is considered to be unimportant as a transporting ligand for U at temperatures higher than 100 °C (Götz et al., 2011; Kalintsev et al., 2021), U-CO_3-bearing aqueous species were suppressed during the modeling.

Many of the important Fe-bearing aqueous and mineral species are included in the default thermo.com.v8.r6+ database within GWB. These comprise $FeCl^+$, $FeCl^{2+}$, $FeCl_{2(aq)}$, $FeCl_4^{2-}$, $FeCO_3^+$, FeF^{2+}, FeF^{2+}, $FeSO_4^+$, pyrite, hematite, goethite and magnetite. However, thermodynamic data for a large number of Fe-bearing species were not included in the default database. Thermodynamic data for these species are reported in Robie and Hemingway (1995), Shock et al. (1997), Sverjensky et al. (1997), Chase (1998), Diakonov et al. (1999), Mercury et al. (2001), Zhao and Pan (2001), Hemingway et al. (2002), Chivot (2004), Liu et al. (2006), Stefánsson (2007), Testemale et al. (2009), Blanc (2017), Stefánsson et al. (2019) and Gammons and Allin (2022). As was the case for the U-bearing species, the thermodynamic data for the Fe-bearing species from these studies were incorporated in the Unitherm database of HCh (Shvarov and Bastrakov, 1999) and used to calculate log K values, which were then integrated into the GWB database. The UNITHERM data.txt and GWB files are provided in in supplementary material (SM5).

Detailed information about the U-bearing and Fe-bearing aqueous species used in the modeling, including relevant reaction equations, log K values at different temperatures, the type of equation of state (EOS) used (HKF or MRB), and the data sources, is provided in the supplementary material SM1 (Table S1). Evaluation of the data from different sources is also provided in SM1 using the log K – T diagrams, and the datasets that are selected to be used in the modeling are marked. Furthermore, various crush tests were conducted to evaluate the sensitivity of parameters used in the modeling, including adoption versus suppression of some species, uncertainties in log K values, and variation in temperature and salinity, which are also included in SM1. Two types of test were conducted: a) use only the predominant and more reliable U- and Fe-bearing aqueous species (i.e., UO_2Cl_2, UO_2Cl^+, UCl_4(aq), $FeCl_4^-$, $FeCl_3$(aq) and $FeCl_4^{2-}$) and suppress other species to evaluate the impact induced by the uncertainties related to the subordinate and less reliable species; and b) use a range of log K values of the predominant species, including UO_2Cl^+, UO_2Cl_2(aq), UCl_4(aq) $FeCl_4^-$ and $FeCl_3$, to evaluate the impact induced by errors in log K estimation. It was found that the subordinate aqueous species and the uncertainties in log K values have insignificant impact on the modeling results. Activity coefficients were calculated using the B-dot equation (Helgeson et al., 1969), as was also used in previous studies of similar fluid systems (Komninou and Sverjensky, 1996). Uncertainties related to this method for high-salinity fluids (Bethke, 2007) were evaluated by comparing models with different salinities; it was found that the variation in salinities (from 18 wt% to 34.1 wt% NaCl equiv.) does not result in significantly different patterns in the pH–log fO_2(g) diagrams (SM1). The water dissociation constant was calculated using the equation of Marshall and Franck (1981).

Solubility diagrams in pH–log fO_2(g) coordinates were constructed using the Phase2 program of the GWB software package. As mentioned by Bethke et al. (2020), Phase2 operates by tracing a series of stacked reaction paths across the diagram and, thus, each point on the Phase2 diagrams represents the complete solution to the equations describing the distribution of mass of the system. The React program of GWB was used to simulate the fluid-rock interactions between U-bearing fluids and major minerals in the host-rocks, including K-feldspar, albite, anorthite, muscovite and biotite. During the fluid-rock interaction simulations, minerals were suppressed unless they have been reported to occur in hydrothermal uranium deposits. The minerals/solids present in hydrothermal uranium deposits and used in the simulation comprise uraninite, hematite, goethite, fluorite, pyrite, illite, quartz, kaolinite, calcite and muscovite.

3. Model setup and modeling results

Two sets of geochemical models were prepared to evaluate the solubility and speciation of U and Fe using the newly compiled database described above. The first set considers hydrothermal fluids of moderate salinity (<15 wt%NaCl equiv.) typically found in volcanic- and granite-related uranium deposits (Bonnetti et al., 2018, 2020; Chi et al., 2020; Guo et al., 2020), and the second considers the basinal brines of high salinity (25–35 wt% NaCl equiv.) typical of unconformity-related uranium deposits (Richard et al., 2016; Chi et al., 2019; Martz et al., 2019). Both sets assume compositions in the system Fe-U-Na-K-Mg-Ca-Cl-C-Al-Si- H-O(—F). The initial fluid composition and P-T conditions, as well as the results of each set of models, are described below.

3.1. Modeling of U and Fe solubility in moderate-salinity hydrothermal fluids

Moderate-salinity (< 15 wt% NaCl equiv.) hydrothermal fluids are commonly trapped as fluid inclusions in volcanic- and granite-related U deposits (Hu et al., 2008, 2009; Dahlkamp, 2009, 2013; Zhang et al., 2021; Chi et al., 2020). The ore-forming fluids are considered to be oxidized (above the MH buffer) based on the association of the uranium mineralization with hematization (Dolníček et al., 2014; Bonnetti et al., 2018, 2020). The homogenization temperatures of the fluid inclusions mostly fall in the range from 150 to 330 °C (Guo et al., 2020; Chi et al., 2020). An abundance of fluorite associated with the uranium mineralization suggests that the ore-forming fluids contained F^-.

The initial composition of the mineralizing fluids used in the modeling was based on LA-ICP-MS analyses of fluid inclusions in ore-stage fluorite and quartz from the Zoujiashan deposit in the Xiangshan volcanic-related uranium deposits (the largest volcanic-related uranium ore field in China) by Yu et al. (2019) (SM2 Table S2). These deposits are hosted mainly by Cretaceous porphyritic lava and granite, and the ores are commonly associated with fluorite in veins and hematite in the host rocks (Guo et al., 2020). The accompanying hydrothermal alteration minerals are hematite, illite, quartz, chlorite, albite, apatite, calcite and sericite, and locally sulfides such as pyrite, molybdenite, chalcopyrite, galena and sphalerite (Yu et al., 2019; Bonnetti et al., 2020). The salinity varies from 5.9 to 13.2% wt% NaCl equiv. (average 9.2% wt% NaCl equiv., corresponding to a chlorinity of ~55 g/kg Cl), and the homogenization temperatures vary from 219 to 279 °C (average 261 °C). Average concentrations of Na, Mg, K, Ca, Fe and U from the LA-ICP-MS analyses normalized to a salinity of 9.2 wt% were used in the modeling (Table 1). As indicated by Hu et al. (2009), the ore-forming fluids in Xiangshan have percent levels of ΣCO_2, so HCO_3^- content is specified as 0.3 mol/kg (equaling to about 1.32%ΣCO_2). A temperature of 250 °C was used for the modeling based on the fluid inclusion homogenization temperatures and a relatively shallow mineralizing environment (thus a small pressure correction). The SO_4^{2-}, $SiO_{2(aq)}$, Al^{3+} and F^- concentrations were buffered by gypsum, quartz, muscovite and fluorite (Table 1), respectively, and were calculated using the SpecE8 program of the GWB

Table 1
Fluid properties used in thermodynamic modeling.

Components	Volcanic-related Zoujiashan U deposit in Xiangshan ore field	Unconformity-related U deposits in Athabasca Basin
Na^+	31,719 ppm	56,225 ppm
Mg^{2+}	666 ppm	20,812 ppm
K^+	4231 ppm	12,901 ppm
Ca^{2+}	695 ppm	25,125 ppm
Fe^{2+}	884 ppm	2257 ppm
UO_2^{2+}	14 ppm	66 ppm
F^-	149 ppm	
SiO_2(aq)	333 ppm	148 ppm
Al^{3+}	0.073 ppm	0.06 ppm
Cl^{-*}	55,620 ppm	206,500 ppm
HCO_3^-	0.3 mol/kg	49 ppm
SO_4^{2-}	0.01 mol/kg	38.4 ppm
Temperature	250 °C	200 °C
Salinity	9.2 NaCl equiv.%	34.1 NaCl equiv.%
Chlorinity	55.62 g/kg	206.5 g/kg

* The Cl concentration is calculated by charge balance.

software package (Bethke, 2007; Bethke et al., 2018).

The modeling results show that U is highly soluble under acidic conditions regardless of the fO_2 (Fig. 1a-b). The isopleths for U in the pH – log fO_2 diagrams generally have positive slopes (Fig. 1a), allowing high U concentrations to be maintained over a wide pH range at relatively oxidizing conditions. At log fO_2 values > −25 (~ MH + 10) and a pH ≤ 4.3, > 10 ppm U can be dissolved in the solution, whereas at log fO_2 < −30 (~ MH + 5), the pH must be <1.5 for the fluid to dissolve >10 ppm U (Fig. 1a). The dominant U-bearing aqueous species are $UO_2Cl_{2(aq)}$ and UO_2Cl^+ under relatively oxidizing conditions (Fig. 1b), and is accompanied by species such as $UO_{2(aq)}^{2+}$, $UO_{2\ (aq)}$ and UO_2F^+ (Fig. 1c). Under relatively reducing and acidic (pH < 1.5) conditions, the dominant U-bearing species is $UCl_{4(aq)}$ (Fig. 1b), and there are minor proportions of UCl_2^{2+}, UO_2Cl^+, UCl^{3+}, and $UO_2Cl_{2(aq)}$ (Fig. 1d). In both cases, the total dissolved U content decreases sharply if pH exceeds a threshold that depends on the fO_2 (red line in Fig. 1c and d). At a fixed pH of 2.5, the total dissolved U concentration is high over a wide range of fO_2 values, above which it decreases precipitously (Fig. 1e). If the pH is extremely low (~ 1), the dissolved U concentration is high at log fO_2 values as low as −40 (~MH-5) (Fig. 1f).

Like U, Fe is also more soluble under acidic conditions. In addition, Fe is mainly present as Fe^{3+}-bearing species ($FeCl_{3(aq)}$ and $FeCl_4^-$) at relatively oxidized conditions and Fe^{2+}-bearing ($FeCl_4^{2-}$) species at relatively reduced conditions (Fig. 2a). At log fO_2 values > −18 (~ MH + 17), an increase in pH to a value around 2.9 leads to precipitation of hematite from Fe^{3+} in the solution, whereas at log fO_2 values < −31 (~ MH + 4), increasing pH results in the precipitation of hematite or magnetite from Fe^{2+} in the solution (Fig. 2a). At log fO_2 values between −18 and − 31, increasing pH results in the transformation of Fe^{3+} to Fe^{2+} in the solution, followed by the precipitation of hematite from Fe^{2+} in the solution (Fig. 2a). For example, at log fO_2 = −25 (~MH + 10), Fe^{3+} species ($FeCl_{3(aq)}$ and $FeCl_4^-$) are dominant at pH < 1.2, but the concentration of Fe^{2+} species ($FeCl_4^{2-}$) increases with pH and become the major Fe-bearing aqueous species when pH increases to >1.2 (Fig. 2b). The solubility of Fe decreases significantly for pH > 3.5 (Fig. 2b).

Superposition of the modeling results of U and Fe solubility indicates that the dominant dissolved U and Fe species depend on both pH and fO_2 (Fig. 2a). Overall, U^{6+} and Fe^{3+} species ($UO_2Cl_2^0$ and $FeCl_3^0$) are dominant at relatively high fO_2 values, U^{4+} and Fe^{2+} species (UCl_4^0 and $FeCl_4^{2-}$) are dominant at relatively low fO_2 values, and U^{6+} and Fe^{2+} species ($UO_2Cl_2^0$ and $FeCl_4^{2-}$) or U^{4+} and Fe^{3+} species (UCl_4^0 and $FeCl_3^0$) are dominant at intermediate fO_2 values (Fig. 2a). At log fO_2 = −10.2 (MH + 25) (Fig. 2c), log fO_2 = −15.2 (MH + 20) (Fig. 2d) and log fO_2 = −20.2 (MH + 15) (Fig. 2e), U^{6+} species are dominant over the pH range from 0 to 8; the solubility of U starts to decrease at pH > ~4.1 and the solubility of Fe decreases sharply at pH > ~2.9 (Fig. 2c, d, e). At log fO_2 = −25.2 (MH + 10) (Fig. 2f), U is dissolved dominantly as U^{6+} species over the pH range from 0 to 8, whereas Fe is dissolved dominantly as Fe^{3+} species at pH < 1.2 and Fe^{2+} at pH >1.2 (Fig. 2f). The solubility of U also starts to decrease at pH > ~2.8 and the solubility of Fe decreases sharply at pH > ~3.6 (Fig. 2f). At log fO_2 = −30.2 (MH + 5) (Fig. 2g), U and Fe are dissolved mainly as U^{4+} and Fe^{3+} species at pH < ~0.1, as U^{4+} and Fe^{2+} species at pH = ~0.1–1.1 and as U^{6+} and Fe^{2+} species at pH > ~1.1; the solubility of U decreases sharply at pH > ~1.5 and the solubility of Fe drops at pH > ~ 4.2 (Fig. 2g). At log fO_2 = −35.2 (MH) (Fig. 2h), U is dissolved dominantly as U^{4+} at pH < ~2.6 and Fe is dissolved as dominantly as Fe^{2+} species over the pH range from 0 to 8; the solubility of U and Fe drops sharply at pH values > ~1.5 and > ~4.8, respectively (Fig. 2h).

In summary, as shown in Fig. 2a, high concentrations of U (from 10 to >100 ppm) and Fe (> 1000 ppm) can be dissolved in acidic (pH < ~2.9) fluids at redox conditions below and above the MH buffer. Iron and U can be co-transported in various combinations of their oxidized and reduced valences. An increase in pH above certain threshold values, which depend on the redox conditions, can cause large decreases in U and Fe solubility, leading to uranium mineralization and hematization.

3.2. Modeling of U and Fe solubility in high-salinity hydrothermal fluids

The modeling of U and Fe solubility in high-salinity hydrothermal fluids was based on information for the basinal brines and ore-forming fluids of the unconformity-related U deposits in the Athabasca Basin. Fluid inclusion data have demonstrated that the deposits formed from fluids in the H_2O-NaCl-$CaCl_2$ system with a salinity of 25–35 wt% and variable Na/Ca ratios that were derived from basinal brines (Richard et al., 2012, 2013, 2016; Chu and Chi, 2016; Wang et al., 2018; Chi et al., 2019; Martz et al., 2019; Rabiei et al., 2021). The ore-forming fluids are inferred to have been oxidizing (above the magnetite-hematite buffer) based on hematization associated with uranium mineralization (Komninou and Sverjensky, 1996; Ng et al., 2013a and b) and to have had a pH <4 based on the alteration mineral assemblage illite-kaolinite (Kotzer and Kyser, 1995; Rozsypal et al., 2009; Richard et al., 2012). The concentrations of Na, Mg, K, Ca, Fe and U in the ore-forming fluids used in the modeling are average values from Richard et al. (2012) (SM3 Table S3), and the salinity, calculated based on charge balance and adopted in the modeling, is 34.1 NaCl equiv.%, corresponding to a chlorinity of ~206.5 g/kg Cl (Table 1). The contents of $SiO_{2(aq)}$ and Al^{3+} were buffered by quartz and muscovite, and the concentrations of SO_4^{2-} and HCO_3^- were taken from Komninou and Sverjensky (1996). The temperature was set at 200 °C (Table 1), and a lower temperature of 150 °C was also tested as a variation study (SM1). These temperatures are within the range of temperature (120 to 200 °C) estimated by Richard et al. (2012) for the ore-forming fluids and are consistent with fluid inclusion homogenization temperatures (Derome et al., 2005; Richard et al., 2012, 2016; Chu and Chi, 2016; Martz et al., 2019; Rabiei et al., 2021) and the small pressure correction required due to the shallow environment of mineralization (Chi et al., 2018).

The modeling results are similar to those reported for the previous model in terms of dissolved species and their relationships to pH and log fO_2 (Figs. 1 and 3 versus Figs. 2 and 4) despite the differences in salinity and temperature. The solubility of U, however, is approximately one order of magnitude higher than for the moderate-salinity model. As in the previous model, U is highly soluble under acidic conditions regardless of the fO_2 value, and fluids with high U contents can develop over a relatively wide pH range (pH ≤ 4.2 for 10 ppm U) under oxidizing conditions. This contrasts with the narrow pH range (pH < 1.8 for 10 ppm U) for which U concentrations are high under reducing conditions (Fig. 3a-b). Similarly, under oxidizing conditions, U is present in the fluid mainly as $UO_2Cl_{2(aq)}$, with minor UO_2Cl^+, UO_2^{2+}, and UO_2OH^+ (Fig. 3c), whereas under reducing conditions, it is present dominantly as $UCl_{4(aq)}$, with minor UCl_2^{2+}, $UO_2Cl_{2(aq)}$, $UO_2Cl^+$and UCl^{3+} (Fig. 3d). In both cases, the total dissolved U content decreases sharply if the pH exceeds a threshold value that depends on fO_2 (red line in Fig. 3c and d). At a fixed pH of 3, the total dissolved U is at a high concentration over a wide range of fO_2 values, and then decreases precipitously with decreasing fO_2 (Fig. 3e). At the extremely low pH of 1, the concentration of dissolved U is high at log fO_2 values as low as −45 (~MH-5) (Fig. 3f).

As is the case for the low to medium salinity fluids, Fe is more soluble under acidic conditions in the high-salinity fluids (Fig. 4a). Iron is mainly present as Fe^{3+}-bearing species ($FeCl_{3(aq)}$ and $FeCl_4^-$) at relatively oxidized conditions and Fe^{2+}-bearing species ($FeCl_4^{2-}$) at relatively reduced conditions (Fig. 4a). At log fO_2 values > −21 (~ MH + 19), an increase in pH from a value of ~3.1 leads to precipitation of hematite from Fe^{3+} in the solution, whereas at log fO_2 values < −33 (~ MH + 7), increasing the pH leads to precipitation of hematite or magnetite from Fe^{2+} in the solution (Fig. 4a). At log fO_2 values between −21 and − 33, increasing pH results initially in the transformation of Fe^{3+} into Fe^{2+} in the solution, and eventually the precipitation of hematite from Fe^{2+} (Fig. 4a). For example, at a log fO_2 of −20 (~MH + 20), Fe^{3+}-bearing species ($FeCl_{3(aq)}$ and $FeCl_4^-$) are the predominant species at pH < 3.2, and $FeCl_4^{2-}$ is the main Fe-bearing aqueous species at pH > 3.2 (Fig. 4b).

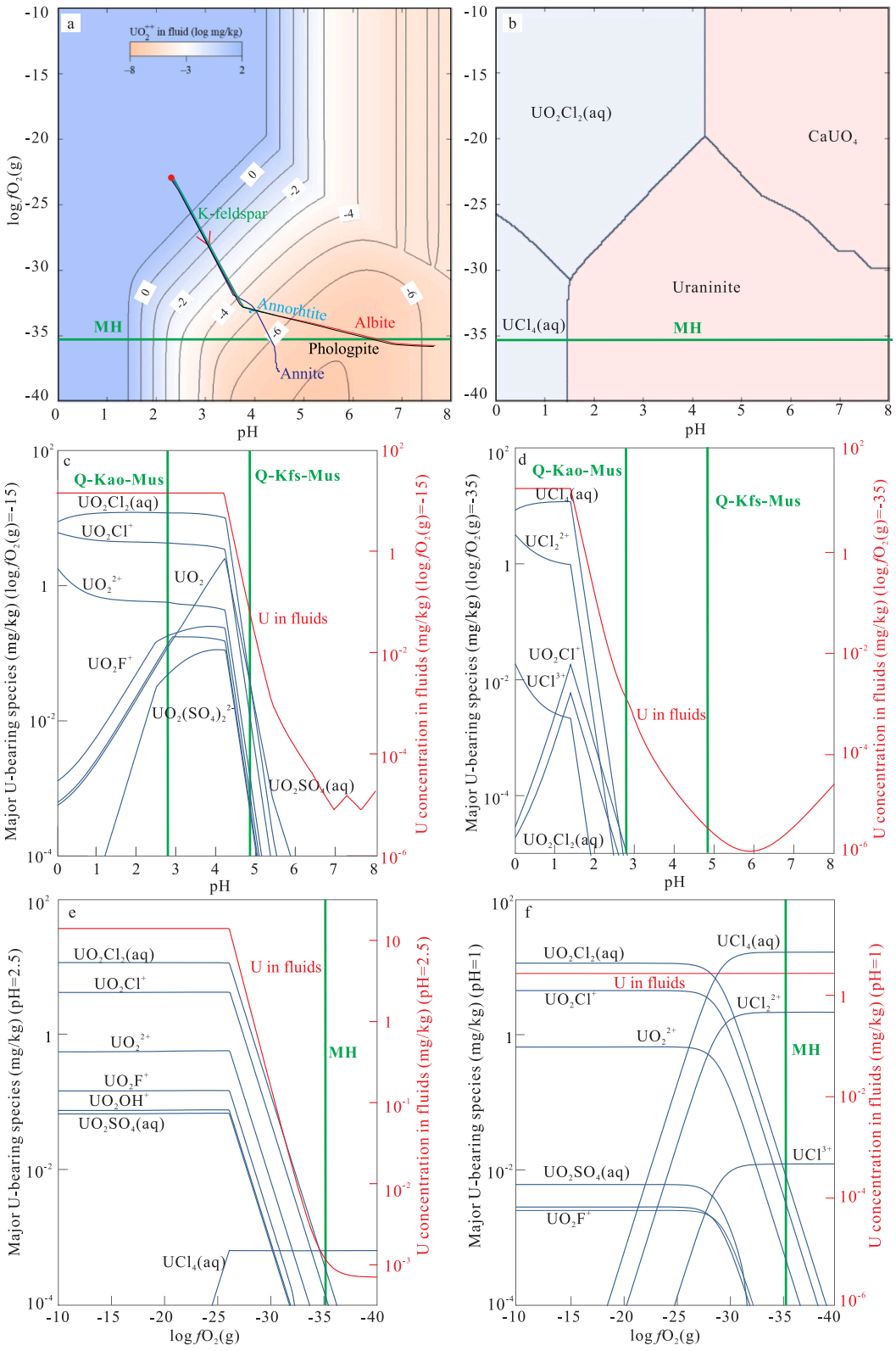


Fig. 1. Uranium solubility and speciation diagrams for the moderate-salinity hydrothermal fluid at 250 °C: pH- fO_2 diagrams for U solubility (a) and U speciation (b). The lines starting from the red dot in the left-up parts represent the traces of fluid rocks interactions in Fig. 5; concentrations of major U-bearing species in the fluid as a function of pH at log fO_2 (g) = −15 (c) and log fO_2 (g) = −35 (d); Concentrations of major U-bearing species in the fluid as a function of fO_2 (g) at pH = 2.5 (e) and pH = 1 (f). The oxygen buffer MH (magnetite-hematite), which is located at a log fO_2 (g) value of −35.2 at 250 °C, is shown in Figs. 1a, b, e and f. The traces of the fluid-rock interactions in the reaction path modeling are shown in (a). (For interpretation of the references to colour in this figure legend, the reader is referred to the web version of this article.)

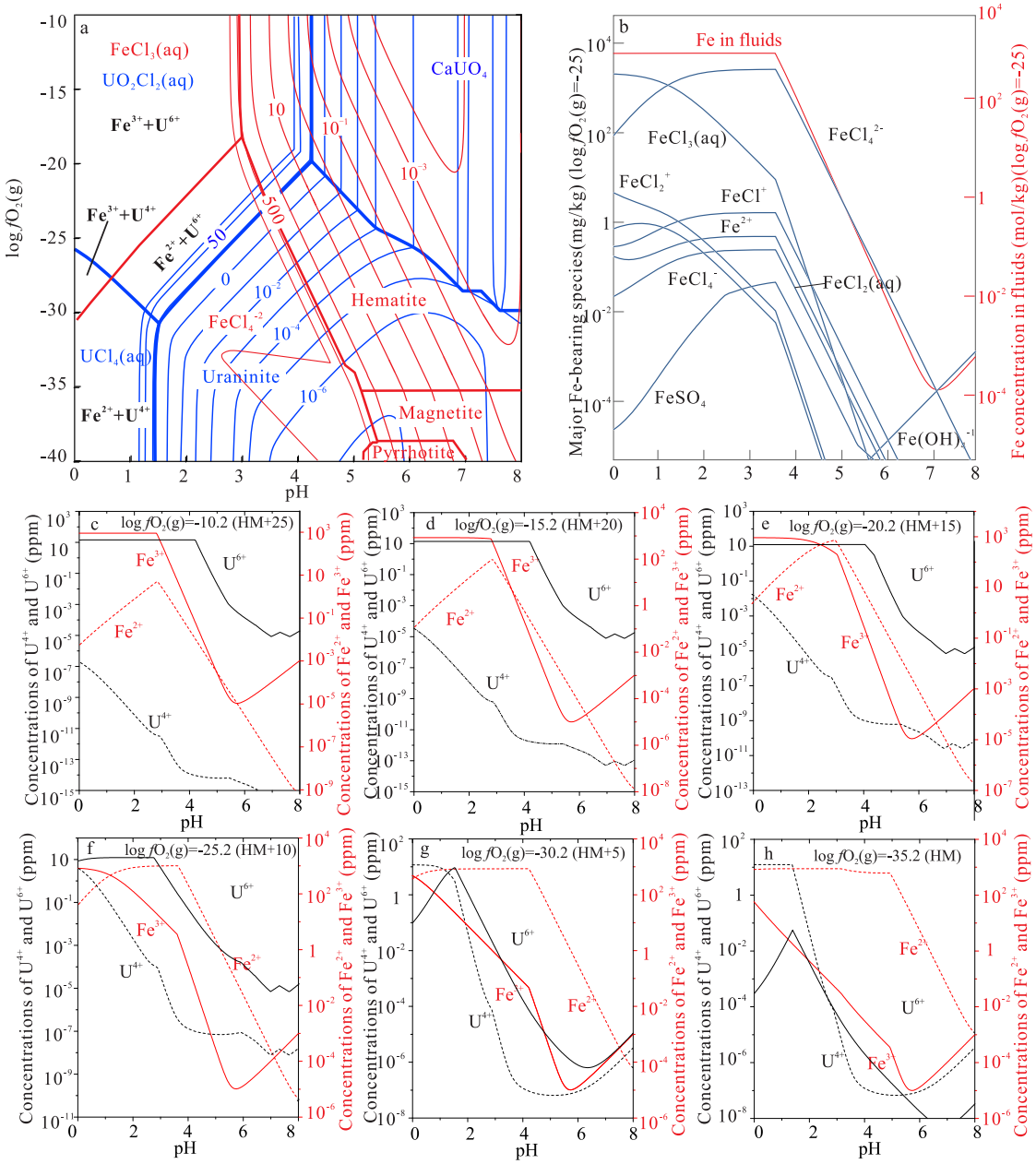


Fig. 2. Iron solubility and speciation diagrams for the moderate-salinity hydrothermal fluid at 250 °C: (a) A log fO_2 - pH diagram for U—Fe solubility and speciation; The red and blue contours indicate the solubility of U and Fe, respectively, and the black chemical symbols indicate the fields of the dominant U and Fe valance states. The contour lines of 50–100 ppm for U were drawn independently by setting the UO_2 concentration of the system to 100 ppm without changing the other parameters. Similarly, the contours of 1000 ppm for Fe were drawn independently by changing the Fe^{2+} concentration in the system to correspond to a total Fe content of 1000 ppm. (b) Concentrations of major Fe-bearing species in the hydrothermal fluid as a function of pH at log $fO_2(g) = -25$ (~HM + 10). The concentrations of Fe^{2+}, Fe^{3+}, U^{6+} and U^{4+} in the hydrothermal fluid as a function of pH at log $fO_2(g)$ = HM + 25 (c), HM + 20 (d), HM + 15 (e), HM + 10(f), HM + 5 (g) and HM (g). (For interpretation of the references to colour in this figure legend, the reader is referred to the web version of this article.)

Superposition of the modeling results of U and Fe solubility demonstrates that both pH and redox conditions control the nature of the dominant dissolved U and Fe species (Fig. 4a). Overall, U^{6+} and Fe^{3+} species ($UO_2Cl_2^0$ and $FeCl_3^0$) are dominant at relatively high fO_2 values, U^{4+} and Fe^{2+} species (UCl_4^0 and $FeCl_4^{2-}$) are dominant at relatively low fO_2 values, and U^{6+} and Fe^{2+} species ($UO_2Cl_2^0$ and $FeCl_4^{2-}$) or U^{4+} and Fe^{3+} species (UCl_4^0 and $FeCl_3^0$) are dominant at intermediate fO_2 values (Fig. 4a). At log $fO_2 = -15.5$ (MH + 25), U is dissolved mainly as U^{6+} species in the pH range from 0 to 8, whereas Fe is dissolved primarily as Fe^{3+} species at pH = 0–4.4 and 6.6–8 and Fe^{2+} species at pH = 4.4–6.6; the solubility of U and Fe begins decreasing at pH > 4 and pH > 2.9, respectively (Fig. 4c). At log $fO_2 = -20.5$ (MH + 20), U is dissolved mainly as U^{6+} species in the pH range from 0 to 8, whereas Fe is dissolved primarily as Fe^{3+} species at pH = 0–3.1 and 7–8 and Fe^{2+} species at pH = 3.1–7; the solubility of U and Fe begins decreasing at pH > 4 and pH > 2.9, respectively (Fig. 4d). At log $fO_2 = -25.5$ (MH + 15), U is dissolved mainly as U^{6+} species in the pH range from 0 to 8, whereas Fe is dissolved primarily as Fe^{3+} species at pH = 0–2 and 7.5–8 and Fe^{2+} species at pH = 2–7.5; the solubility of U and Fe begins decreasing at pH > 3.6 and pH > 3.3, respectively (Fig. 4e). At log $fO_2 = -30.5$ (MH + 10), U is dissolved mainly as U^{4+} species at pH < 0.9 and U^{6+} species at pH > 0.9, whereas Fe is dissolved mainly as Fe^{3+} species at pH < 0.7 and Fe^{2+} species at pH > 0.7; the solubility of U and Fe begins to decrease at pH > 2.3 and pH > 4, respectively (Fig. 4f). At log $fO_2 = -35.5$ (MH + 5)

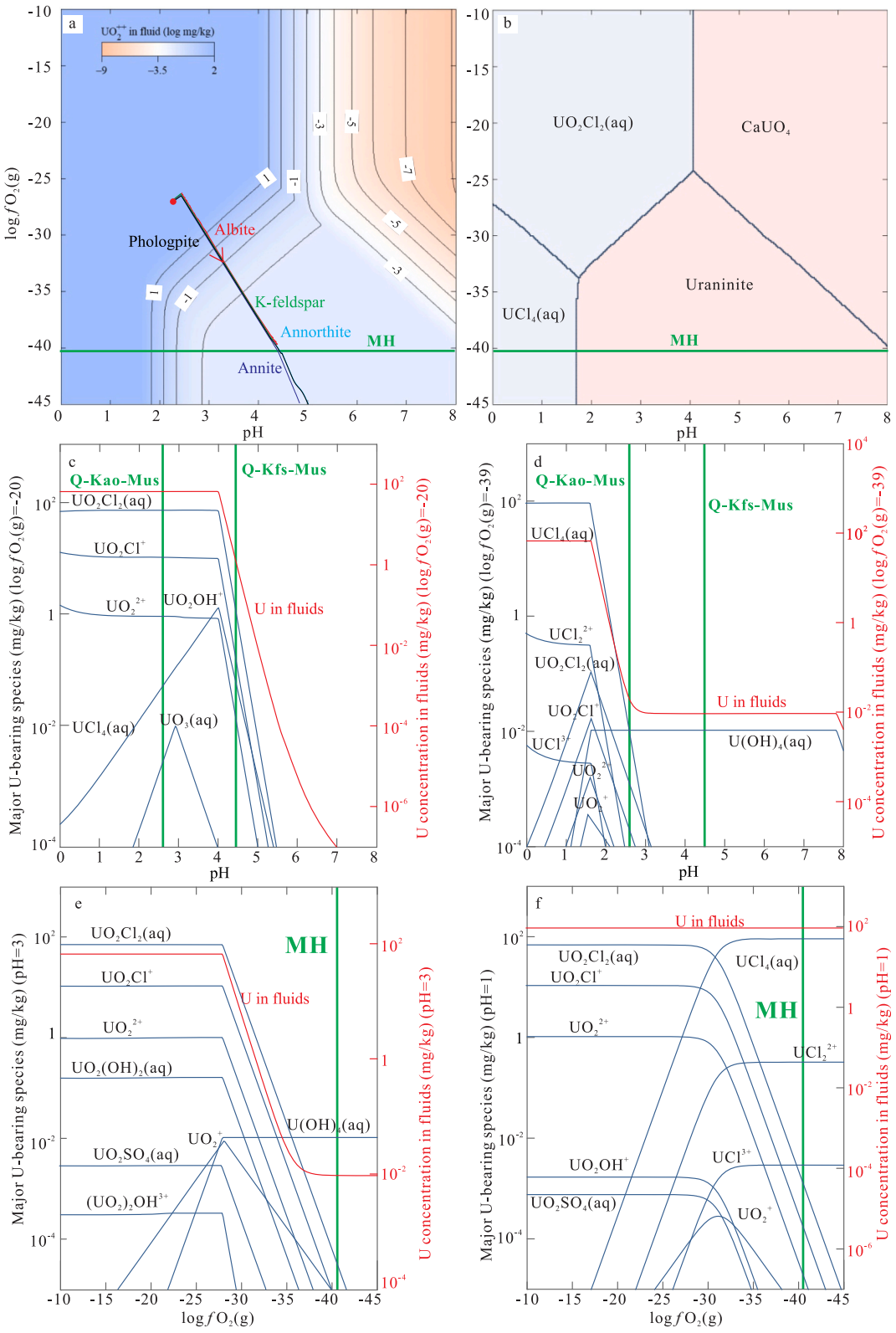


Fig. 3. Uranium solubility and speciation diagrams for high-salinity hydrothermal fluids at 200 °C: pH-fO_2 diagrams for U solubility (a) and U speciation (b). The lines starting from the red dot in the left-up parts represent the traces of fluid rocks interactions in Fig. 6; Concentrations of major U-bearing species in the hydrothermal fluid as a function of pH at log fO_2(g) = −25 (c) and log fO_2(g) = −45 (d); Concentrations of major U-bearing species in the fluid as a function of fO_2(g) at pH = 3 (e) and pH = 1 (f). The oxygen buffer MH (magnetite-hematite), which is located at a log fO_2(g) value of −46.9 at 200 °C, is shown in Figs. 3a, b, e and f. The traces of the fluid-rock interactions in the reaction path modeling are shown in (a). (For interpretation of the references to colour in this figure legend, the reader is referred to the web version of this article.)

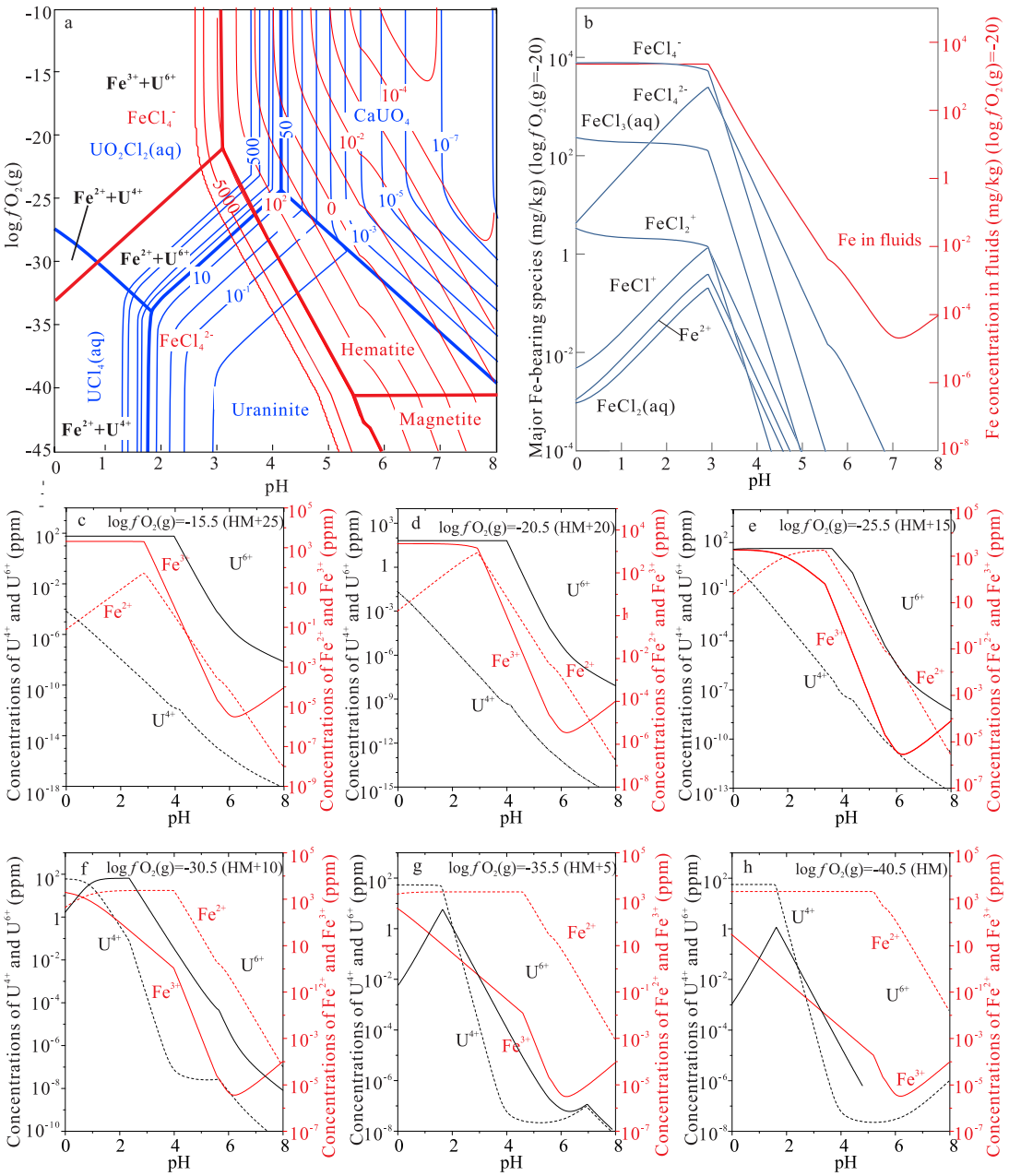


Fig. 4. Iron solubility and speciation diagrams for high-salinity hydrothermal fluids at 200 °C: (a) A pH-fO_2 diagram for Fe solubility and speciation. The red and blue contours indicate the solubility of U and Fe, respectively, and the black chemical symbols indicate the fields of the dominant U and Fe valance states. The contour lines of 50–10^3 ppm for U were drawn independently by setting the UO_2 concentration of the system to 100 ppm without changing the other parameters. Similarly, the contour lines of 5000–10^4 ppm for Fe were drawn independently by changing the Fe^{2+} concentration in the system to correspond to a total Fe content of 10,000 ppm. (b) Concentrations of major Fe-bearing species in the fluid as a function of pH at log $fO_2(g) = -20$. The concentrations of Fe^{2+}, Fe^{3+}, U^{6+} and U^{4+} in hydrothermal fluid as a function of pH at log $fO_2(g)$ = HM + 25 (c), HM + 20 (d), HM + 15 (e), HM + 10(f), HM + 5 (g) and HM (g). (For interpretation of the references to colour in this figure legend, the reader is referred to the web version of this article.)

and − 40.5 (MH), the solubility of U and Fe starts to decrease at pH > 1.6 and pH > 4.7–5.2, respectively (Fig. 4g-h).

As shown in Fig. 4a, 10 to >1000 ppm U and > 1000 ppm Fe can be dissolved in oxidized (fO_2 > MH + 8) and acidic (pH < 3.7) fluids at variable redox conditions below and above the MH buffer. The modeling results at 150 °C (SM1) show similar patterns as those at 200 °C (Fig. 4), although U and Fe concentrations are lower at 150 °C than at 200 °C (SM1). Therefore, for the high-salinity fluids, Fe and U can be co-transported in various combinations of oxidized and reduced species, as is the case for the medium-low salinity fluids. Similarly, an increase in pH across a threshold value can cause a sharp decrease in U and Fe solubility, resulting in uranium mineralization and hematization.

3.3. Modeling of fluid-rock interaction related to U and Fe precipitation

The modeling results described above indicate that U^{6+} and Fe^{2+} can be co-transported in hydrothermal fluids of moderate to high salinity. Changes in either fO_2 or pH, or a combination of them, can result in the precipitation of uraninite and hematite. In order to understand the processes which may produce these changes, fluid-rock reaction path modeling was conducted using minerals that are commonly present in the host rocks of volcanic-hosted and unconformity-related U deposits, namely albite, K-feldspar, anorthite, muscovite, phlogopite (Mg-end member of biotite) and annite (Fe-end member of biotite). The fluid compositions and thermal conditions were the same as those employed

in the modeling described above and are listed in Table 1. Low pH values (3.3 for the moderate-salinity fluid and 3 for the high-salinity fluid) were assigned to the initial fluid to facilitate clay alteration and promote the solubility of Fe, and high log fO_2 values (−23 or MH + 12.2 for the moderate-salinity fluid and − 27 or MH + 13.5 for the high-salinity fluid) were assumed to promote hematization. The extent of fluid-rock reaction was simulated by titrating the minerals (to a maximum of 200 g for the moderate-salinity fluid and 20 g for the high-salinity fluid) into 1 kg fluid.

The results of the fluid-rock reaction path modeling show that there is a general trend of increasing pH and decreasing fO_2(g) with increasing degree of fluid-rock reaction, for both the moderate-salinity fluid (Fig. 5) and the high-salinity fluid (Fig. 6). Reactions of the moderate-salinity fluid with feldspar cause uraninite to begin precipitating when the pH increases to above ~3.3 and log fO_2(g) decreases to lower than ~ −23 (~MH + 12). Approximately 99% of the U had deposited after the pH increased to ~3.8 and log fO_2(g) decreased to ~ − 27 (~MH + 8). During these fluid-rock interactions, Fe begins precipitating as hematite at a pH of ~3.3 and log fO_2(g) of −23 (~HM + 12). Over 99% of Fe had precipitated by reacting with anorthite, albite and phlogopite which caused the pH reached ~5.8 and log fO_2(g) decreased to ~ −35 (~HM) (Fig. 5b-d). However, the reaction with K-feldspar can only deposit about 88% of Fe with pH increasing to 5.1 and log fO_2(g) decreased to ~ −34 (~HM-1) (Fig. 5a). The reaction with annite and phlogopite causes uraninite precipitation, starting at a pH > 3.3 and log fO_2(g) < −23 (~HM + 12), and ~ 99% of the U had deposited after the pH increased

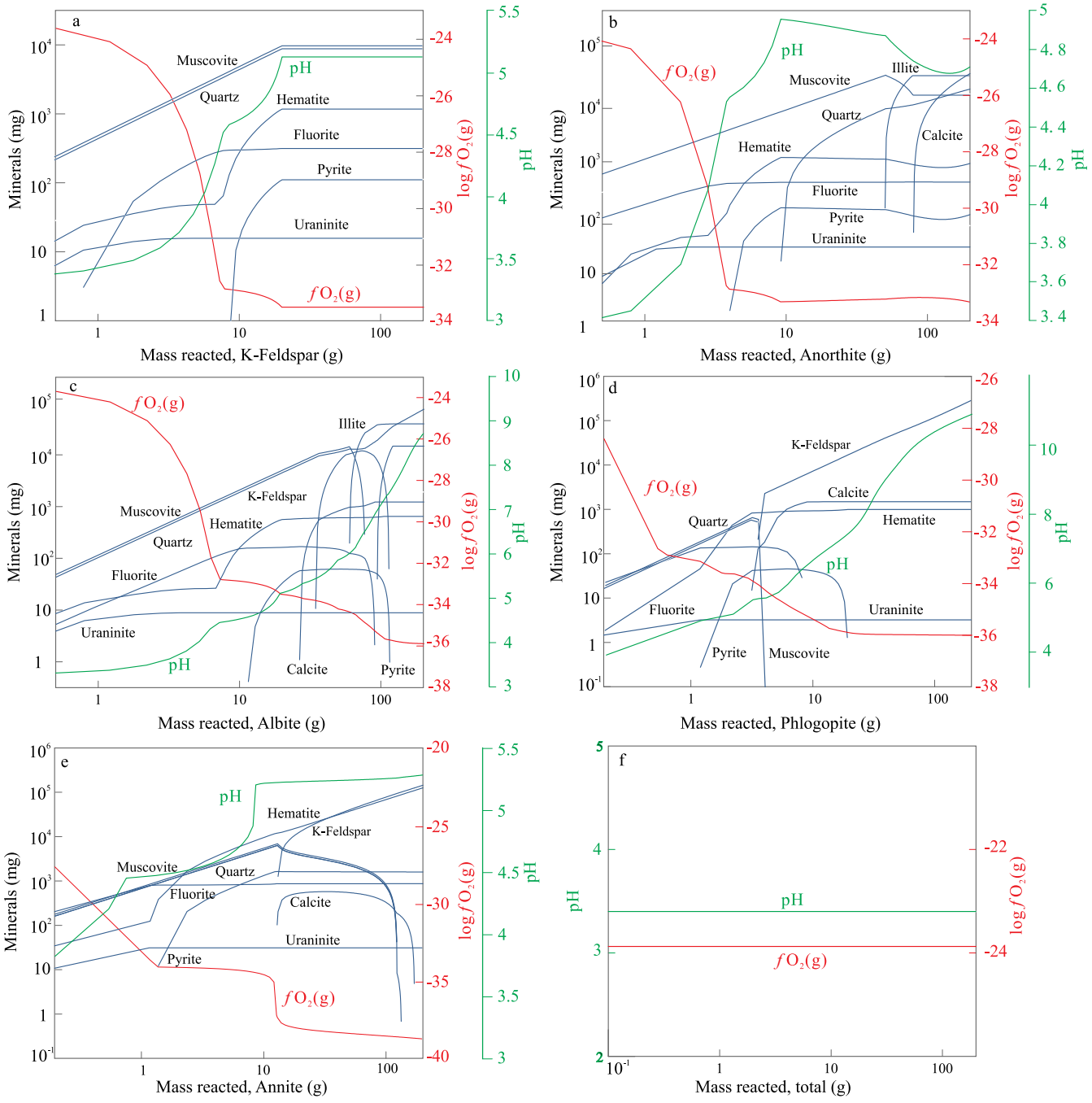


Fig. 5. Diagrams illustrating the progress of reactions involving 1 kg of a moderate-salinity hydrothermal fluid to which a mineral is added in successive 1 g aliquots at 250 °C (Table 1). (a) K-feldspar, (b) anorthite, (c) albite, (d) phlogopite (Mg-end member of biotite), (e) annite (Fe-end member of biotite) and (f) muscovite.

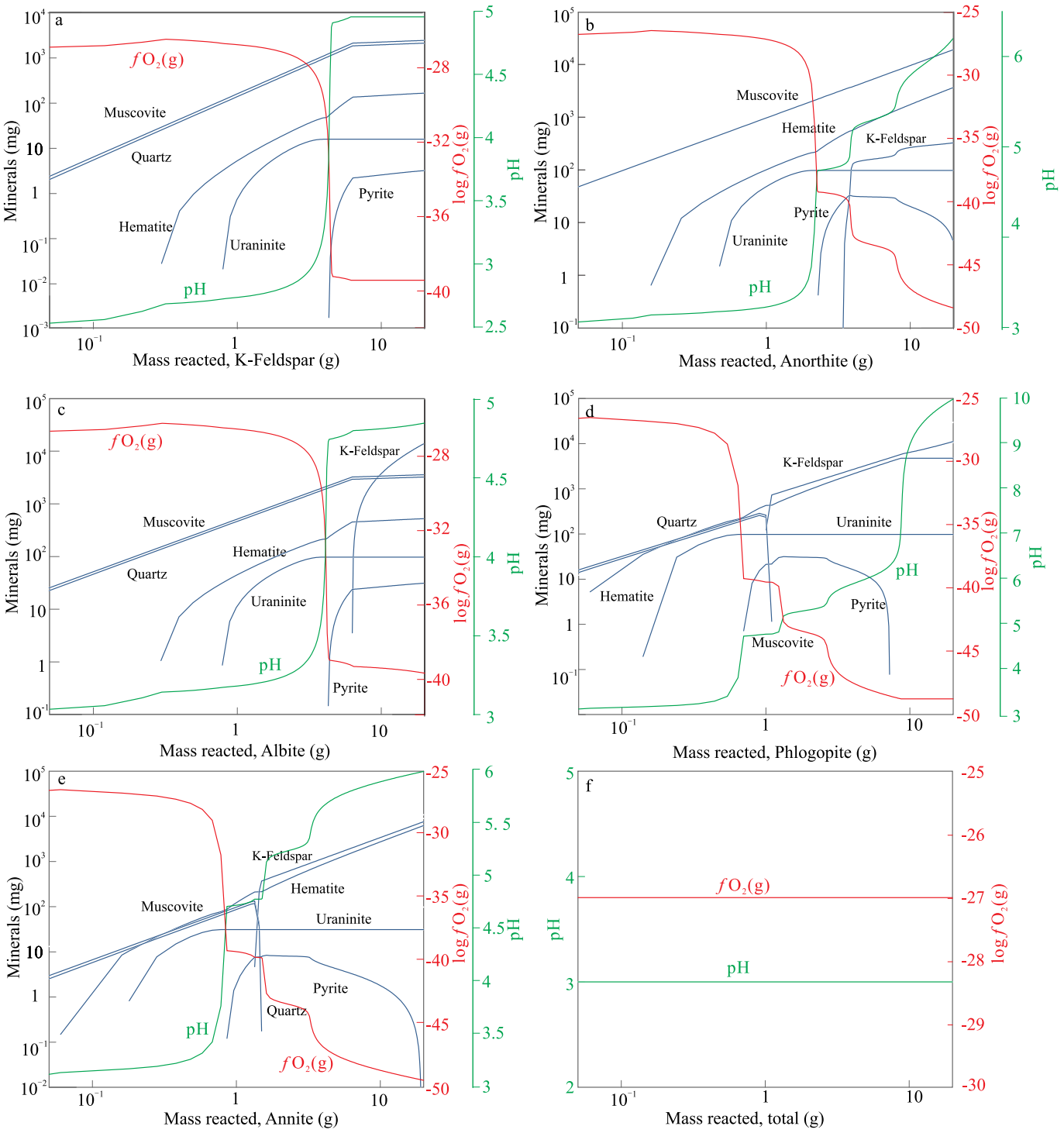


Fig. 6. Reaction path modeling diagrams showing reaction progress between 1 kg of high-salinity hydrothermal fluid at 200 °C (Table 1) and (a) K-feldspar, (b) anorthite, (c) albite, (d) phlogopite (Mg-end member of biotite), (e) annite (Fe-end member of biotite) and (f) muscovite.

to 4.5 and log fO_2(g) decreased to −33 (~MH + 2). The deposition of hematite began at the start of fluid-rock interaction, and the amount precipitated from the reaction with annite was greater than in the other reactions (Fig. 5e). Reaction of the fluid with muscovite does not cause U precipitation because of no changes in pH and log fO_2 (Fig. 5f). The traces of the fluid-rock interactions are show in Fig. 1a.

The interaction of the high-salinity fluid with feldspar and phlogopite leads to U and Fe precipitation when pH increases to ~3.2 and log fO_2(g) decreases to ~ −27 (~MH + 13). Over 99% of U had precipitated after pH increased to ~3.6 and log fO_2(g) decreased to −30 (~MH + 10), respectively (Fig. 6 a-d). During reaction with annite, uraninite precipitation starts at pH > 3.2 and log fO_2(g) < −27 (~HM + 13), and about 99% of U had deposited after pH increased to 3.4 and log fO_2(g) decreased to −29 (~MH + 11). As with the moderate-salinity fluid, the deposition of hematite begins at the start of fluid-rock interaction, and the amount of hematite precipitated is greatest for the reaction with annite due to its Fe-bearing nature (Fig. 6e). Similarly, reaction of the fluid with muscovite does not cause U precipitation because of no changes in pH and log fO_2 (Fig. 6f). The traces of the fluid-rock interactions are show in Fig. 3a.

4. Discussion

The results of this study show that high concentrations of U and Fe can be co-transported at equilibrium as mixtures of oxidized and reduced valence species for a wide range of pH and fO_2 conditions. Most significantly, considerable amounts of U^{6+} and Fe^{2+} can be co-transported, in contrast to the findings of Romberger (1984) that U and Fe cannot be co-transported (SM4), which have strongly influenced genetic models for hydrothermal uranium deposits.

Co-transportation of U^{6+} and Fe^{2+} can take place over a wide range of redox conditions ($\log fO_2$ from MH + 35 to MH + 5, Figs. 1-4) and pH values < ~3.3. In contrast, co-transportation of U^{4+} and Fe^{2+} is limited to reducing conditions ($\log fO_2 < -33$ at 250 °C, Figs. 1a-b, 2a-b; $\log fO_2 < -36$ at 200 °C, Figs. 3a-b, 4a-b) and extremely low pH values (<1.5). It therefore follows that co-transportation of U and Fe in nature likely occurs under relatively oxidizing conditions as the U^{6+} and Fe^{2+} species, respectively. Support for this conclusion is provided by the common association of hematization and U mineralization (e.g., Ng et al., 2013a, 2013b; Bonnetti et al., 2018, 2020; Xing et al., 2018, 2019; Chi et al., 2020). Although the results of this study agree with the consensus that U is transported in oxidizing hydrothermal fluids (Romberger, 1984; Komninou and Sverjensky, 1996; Richard et al., 2012; Dargent et al., 2015; Xing et al., 2018, 2019), they differ on the issue of the reduction of U^{6+} to U^{4+} to form uraninite. Whereas previous studies have concluded that uraniferous fluids form uraninite deposits as a result of their interaction with external reductants, the results of our study show that a potential reducing agent, Fe^{2+}, can be transported with U^{6+}. Consequently, U^{6+} could be reduced to U^{4+} by Fe^{2+} and precipitated as uraninite without the need for an external reducing agent, as shown by the fluid-rock interactions the reaction below:

$$UO_2Cl_{2(aq)} + 3H_2O + 2FeCl_4^{2-} = UO_2\ (\text{uraninite}) + Fe_2O_3\ (\text{hematite}) + 10Cl^- + 6H^+ \quad (1)$$

Some studies (Bastrakov et al., 2010. Xing et al., 2018) proposed that H_2O itself could be a potential reducing agent for uranium precipitation through the reaction below:

$$UO_2Cl_{2(aq)} + H_2O = UO_2\ (\text{uraninite}) + 2\ Cl^- + 2H^+ + 1/2O_2(g) \quad (2)$$

However, an increase in $O_2(g)$ would hinder further uranium precipitation, as predicted by Figs. 1a and 3a. In order to drive reaction 2 to the right and precipitate significant amounts of uraninite, O_2 must be continuously consumed, which will need a different reducing agent than H_2O. The consumption of O_2 is indeed demonstrated by the decrease in $\log fO_2(g)$ with increasing fluid-rock interactions (Figs. 5-6), supporting the notion that a reducing agent other than H_2O is required to precipitate uraninite.

Two changes in physicochemical conditions that could lead to U mineral deposition via the reaction 1 are a decrease in temperature and an increase in pH. Additionally, based on the large increase in log K for these reactions which occurs as temperature decreases from 250 °C to 100 °C (from −12.7 to −1.9 for the reaction 1), cooling is an extremely effective driver of U mineral deposition. The same conclusion applies if the U is transported as $UCl_{4(aq)}$ (Timofeev et al., 2018).

According to reaction 1, increasing pH favors precipitation of uraninite, which is consistent with the modeling results presented in Figs. 1 and 3. In highly oxidizing and acidic fluids in which U^{6+} and Fe^{3+} are co-transported, an increase in pH would lead to the transformation of Fe^{3+} to Fe^{2+} (Figs. 2a and 4a) and, in turn, the reduction of U^{6+} to U^{4+} and the precipitation of U oxides. Such an increase in pH is an inevitable consequence of the fluid-rock reactions that consume H^+ by altering minerals like feldspars and biotite to clay minerals such as illite and kaolinite. This effect is also clearly illustrated in Figs. 5 and 6, where precipitation of U oxides is closely associated with a pH increase and the formation of illite. We therefore conclude that, if U^{6+} and Fe^{2+} are co-transported, the redox reactions which convert them to U^{4+} and Fe^{3+}, i.e., co-precipitation of uranium oxides and hematite, are triggered by alteration of the host rocks to clay minerals, and the decrease in fO_2 (Figs. 5 and 6) is the consequence of a pH increase rather than the cause of U precipitation.

In addition to buffering pH, alteration of feldspars and biotite to clay minerals may also contribute to the precipitation of U oxides and hematite kinetically, as is common for redox reactions (Bethke, 2007). Results of experiments suggest that dissolved Fe^{2+} may not be an efficient agent for reducing U^{6+} to U^{4+} (Liger et al., 1999; Dargent et al., 2015), although this kinetic effect may be much less significant at the elevated temperatures of hydrothermal uraninite deposition (Bethke, 2007; Lasaga, 2014). Moreover, redox reactions have been shown to proceed rapidly at the mineral-fluid interface even at low temperature (Ilton et al., 2004). Indeed, a recent study by Pan et al. (2021) suggests that U^{6+} species could initially precipitate with amorphous or microcrystalline silica via surface sorption; the amorphous and microcrystalline silica subsequently transforms to quartz and the U^{6+} is reduced to uraninite through reaction with reducing agents. Minerals such as ferric oxide, clays and mica can adsorb both Fe^{2+} and U^{6+} on their surfaces, thereby concentrating elements and promoting electron transfer (Chakraborty et al., 2010). This process, referred to as coupled sorption-reduction (Allen and Wood, 1988; Villa-Alfageme et al., 2015), could catalyze the reduction kinetics and therefore significantly accelerate chemical reactions (Borovec, 1981; Ilton et al., 2005). In addition, hydrothermal experiments have demonstrated that colloidal suspensions of hematite can form the Fe^{2+} monohydroxo surface complex ($\equiv Fe^{III}OFe^{II}OH^0$), which provides a favorable coordination environment for electrons to be removed from Fe^{2+} (Liger et al., 1999). Since hematite is a product in reaction 1, it could self-catalyze the redox reactions. We therefore conclude that the potential kinetic barriers to redox reaction 1 may be overcome by the formation of hematite and clay minerals.

The physiochemical conditions for the co-transportation and co-precipitation of U and Fe revealed in this study have important implications for U mineralization. For U deposits associated with hematization in jasper-quartzite (Volzhin and Korolev, 1982; Goswami et al., 2019) and leucogranite (Liang et al., 2017), the problem of the low abundance of Fe^{2+}-rich minerals in the host rocks required for U mineralization in conventional models, may be overcome by the co-transportation of Fe^{2+} and U^{6+} in the ore fluids. This process may also explain the non-selective development of the so-called hematite-type U ores in volcanic- and granite-related uranium deposits (Hu et al., 2008; Cuney and Kyser, 2015; Yu et al., 2019; Guo et al., 2020). Such uranium mineralization may be further facilitated by the alteration of feldspars and mafic silicate minerals to clay as discussed above; illite is a common alteration mineral in volcanic- and granite-hosted uranium deposits (Bonnetti et al., 2018, 2020; Chi et al., 2020; Zhang et al., 2021).

In the case of unconformity-related uranium deposits, the results of this study may shed light on the debate about the source of the U. Some researchers have suggested that the U was mainly sourced from the sediments in the basin because the oxidizing conditions, high permeability and availability of brines in the basin are favorable for the extraction and transport of U (Hoeve and Sibbald, 1978; Kotzer and Kyser, 1995; Komninou and Sverjensky, 1996; Fayek and Kyser, 1997; Chi et al., 2019; Wang et al., 2021). Others, however, have concluded that the U was more likely sourced from the basement because U concentrations in the basement rocks are generally higher than in the sedimentary rocks in the basin (Derome et al., 2005; Richard et al., 2010; Martz et al., 2019). It is also possible that the two sources are not exclusive of each other, and that some of the U may have been derived from the basement while the majority may be from the basin (Chi et al., 2019). One of the obstacles to a basement source for the U has been that the relatively reducing nature (compared with sediments in the basin) of the environment imposed by the large proportion of ferrous iron-bearing minerals is unfavorable for U extraction. However, the results of the present study show clearly that U is mobile as U^{6+} even if high

concentrations of Fe^{2+} are present in the fluid.

The evidence that U^{6+} can be transported with a reducing agent like Fe^{2+} greatly increases the range of geological conditions under which U can be transported and deposited. Although the availability of external reducing agents clearly promotes U mineralization (Wersin et al., 1994; Bray et al., 1988; Ng et al., 2013a, 2013b; Derome et al., 2005; Richard et al., 2010; Dargent et al., 2015; Song et al., 2022), it should not be considered a prerequisite for the formation of an economic uranium deposit. On the contrary, the results of our study show that even in the absence of an external reducing agent, there can be significant uranium mineralization and that intense hematization and clay alteration may be important indicators of the presence of a potentially economic uranium resource.

5. Conclusions

The results of the chemical modeling presented in this study, based on the most recent thermodynamic data for U and Fe minerals and dissolved species, indicate that high concentrations of U and Fe can be dissolved in acidic (pH < ~3.3) hydrothermal fluids of moderate to high salinity, over a wide range of redox conditions above and below the magnetite-hematite (MH) oxygen fugacity buffer. They also show that U^{6+} and Fe^{2+} can be co-transported in equilibrium by hydrothermal fluids of moderate to high salinities under acidic and oxidizing conditions. Uranium mineral deposition and associated hematization can take place in response to a pH increase without the participation of reducing agents external to the ore fluids. The most likely cause of such a pH increase is the alteration of minerals in the host rocks, especially feldspars. Clay minerals and hematite also play important roles as catalysts that reduce the kinetic barriers for the redox reactions and promote U mineral precipitation through coupled sorption-reduction. The results of this study can be used to explain the presence of uranium mineralization in rocks that are apparently deficient in reducing agents, as well as the difficulty of U extraction and transport in apparently reducing environments dominated by ferrous Fe in minerals. These findings also expand the range of geological environments for U mineralization, and suggest that the combination of clay alteration and hematization may be used as a uranium mineralization vector if there is evidence for presence of uraniferous fluids.

Supplementary data to this article can be found online at https://doi.org/10.1016/j.chemgeo.2023.121432.

Declaration of Competing Interest

The authors declare that they have no known competing financial interests or personal relationships that could have appeared to influence the work reported in this paper.

Data availability

Data will be made available on request.

Acknowledgments

This work was co-founded by the National Natural Science Foundation of China (42002090; 42172329; 41930428), NSERC (RGPIN-2018-06458), Jiangxi Double Thousand Plan (SQJH2019XDR), and Open Research Fund Program of State Key Laboratory of Nuclear Resources and Environment, East China University of Technology (No. NRE1915). Editorial handling by Dr. Hailiang Dong is gratefully acknowledged. Thorough reviews by Dr. Artas Migdisov, Dr. Yuanming Pan and Dr. Evgeniy Bastrakov greatly improved the manuscript, for which we are thankful.

References

Allen, C., Wood, M., 1988. Bentonite in nuclear waste disposal: A review of research in support of the basalt waste isolation project. Appl. Clay Sci. 3 (1), 11–30.
Anderson, G., Castet, S., Schott, J., Mesmer, R.J.G.e.C.A., 1991. The density model for estimation of thermodynamic parameters of reactions at high temperatures and pressures, 55 (7), 1769–1779.
Bastrakov, E.N., Jaireth, S., Mernagh, T.P., 2010. Solubility of uranium in hydrothermal fluids at 25 to 300 °C. Geosci. Austral. Rec. 1–91.
Bethke, C.M., 2007. Geochemical and Biogeochemical Reaction Modeling. Cambridge University Press, pp. 1–842.
Bethke, C., Farrell, B., Yeakel, S., 2018. The Geochemist's Workbench® Release 12, GWB Essentials Guide; Aqueous Solutions. LLC, Champaign, IL, pp. 1–186.
Bethke, C., Farrell, B., Yeakel, S., 2020. The Geochemist's Workbench® Release 12–GWB Reaction Modeling Guide. In: Aqueous Solutions. LLC Champaign, Illinois, pp. 1–198.
Blanc, P., 2017. Thermoddem: Update for the 2017 Version, Report BRGM/RP-66811-FR.
Bonnetti, C., Liu, X., Mercadier, J., Cuney, M., Deloule, E., Villeneuve, J., Liu, W., 2018. The genesis of granite-related hydrothermal uranium deposits in the Xiazhuang and Zhuguang ore fields, North Guangdong Province, SE China: Insights from mineralogical, trace elements and U-Pb isotopes signatures of the U mineralisation. Ore Geol. Rev. 92, 588–612.
Bonnetti, C., Liu, X., Cuney, M., Mercadier, J., Riegler, T., Yu, C., 2020. Evolution of the uranium mineralisation in the Zoujiashan deposit, Xiangshan ore field: implications for the genesis of volcanic-related hydrothermal U deposits in South China. Ore Geol. Rev. 122, 1–24.
Borovec, Z., 1981. The adsorption of uranyl species by fine clay. Chem. Geol. 32 (1), 45–58.
Bray, C.J., Spooner, T.C., Longstaffe, F.J., 1988. Unconformity-related uranium mineralization, McClean deposits, North Saskatchewan, Canada; hydrogen and oxygen isotope geochemistry. Can. Mineral. 26 (2), 249–268.
Chakraborty, S., Favre, F., Banerjee, D., Scheinost, A.C., Mullet, M., Ehrhardt, J.J., Brendle, J., Vidal, L., Charlet, L., 2010. U(VI) Sorption and Reduction by Fe(II) Sorbed on Montmorillonite. Environ. Sci. Technol. 44 (10), 3779–3785.
Chase, M., 1998. NIST-JANAF Thermochemical Tables. J. Phys. Chem. Ref. Data 1963.
Chi, G., Li, Z., Chu, H., Bethune, K., Quirt, D., Ledru, P., Normand, C., Card, C., Bosman, S., Davis, W., 2018. A shallow-burial mineralization model for the unconformity-related uranium deposits in the Athabasca Basin. Econ. Geol. 113 (5), 1209–1217.
Chi, G., Chu, H., Petts, D., Potter, E., Jackson, S., Williams-Jones, A., 2019. Uranium-rich diagenetic fluids provide the key to unconformity-related uranium mineralization in the Athabasca Basin. Sci. Rep. 9 (1), 1–10.
Chi, G., Ashton, K., Deng, T., Xu, D., Li, Z., Song, H., Liang, R., Kennicott, J., 2020. Comparison of granite-related uranium deposits in the Beaverlodge district (Canada) and South China – A common control of mineralization by coupled shallow and deep-seated geologic processes in an extensional setting. Ore Geol. Rev. 117, 1–16.
Chivot, J., 2004. Thermodynamique des Produits de Corrosion: Fonctions Thermodynamiques, Diagrammes de Solubilité, Diagrammes E-pH des Systemes Fe-H2O, Fe-CO2-H2O, Fe-S-H2O, Cr-H2O et Ni-H2O en Fonction de la Température. Andra, p. 141 (in French).
Chu, H., Chi, G., 2016. Thermal profiles inferred from fluid inclusion and illite geothermometry from sandstones of the Athabasca basin: Implications for fluid flow and unconformity-related uranium mineralization. Ore Geol. Rev. 75, 284–303.
Cumberland, S.A., Douglas, G., Grice, K., Moreau, J.W., 2016. Uranium mobility in organic matter-rich sediments: a review of geological and geochemical processes. Earth Sci. Rev. 159, 160–185.
Cuney, M., 2009. The extreme diversity of uranium deposits. Mineral. Deposita 44 (1), 3–9.
Cuney, M., Kyser, K., 2015. Geology and Geochemistry of Uranium and Thorium Deposits. Mineralo. Assoc. Canada 52 (1), 362.
Dahlkamp, F.J., 2009. Part II: Uranium in Asia–Overview. Uranium Deposits of the World, pp. 453–478.
Dahlkamp, F.J., 2013. Uranium Ore Deposits. Springer Science & Business Media, pp. 1–460.
Dargent, M., Dubessy, J., Truche, L., Bazarkina, E.F., Nguyen-Trung, C., Robert, P., 2013. Experimental study of uranyl(VI) chloride complex formation in acidic LiCl aqueous solutions under hydrothermal conditions (T = 21 °C ~ 350 °C, Psat) using Raman spectroscopy. Eur. J. Mineral. 25, 765–775.
Dargent, M., Truche, L., Dubessy, J., Bessaque, G., Marmier, H., 2015. Reduction kinetics of aqueous U(VI) in acidic chloride brines to uraninite by methane, hydrogen or C-graphite under hydrothermal conditions: Implications for the genesis of unconformity-related uranium ore deposits. Geochim. Cosmochim. Acta 167, 11–26.
Derome, D., Cathelineau, M., Cuney, M., Fabre, C.C., Lhomme, T.R.S., Banks, D.A., 2005. Mixing of sodic and calcic brines and uranium deposition at McArthur River, Saskatchewan, Canada: a Raman and laser-induced breakdown spectroscopic study of fluid inclusions. Econ. Geol. 100 (8), 1529–1545.
Diakonov, I.I., Schott, J., Martin, F., Harrichourry, J.-C., Escalier, J., 1999. Iron (III) solubility and speciation in aqueous solutions. Experimental study and modelling: part 1. Hematite solubility from 60 to 300 C in NaOH–NaCl solutions and thermodynamic properties of Fe (OH) 4−(aq). Geochim. Cosmochim. Acta 63 (15), 2247–2261.
Dolníček, Z., René, M., Hermannová, S., Prochaska, W., 2014. Origin of the Okrouhlá Radouň episyenite-hosted uranium deposit, Bohemian Massif, Czech Republic: fluid inclusion and stable isotope constraints. Mineral. Deposita 49 (4), 409–425.

Fayek, M., Kyser, T.K., 1997. Characterization of multiple fluid. Flow events and rare. Earth. Element mobility associated with formation of of unconformity-type uranium deposits in the Athabasca Basin, Saskatchewan. Can. Mineral. 35 (3), 627–658.
Gammons, C.H., Allin, N.C., 2022. Stability of aqueous Fe (III) chloride complexes and the solubility of hematite between 150 and 300° C. Geochim. Cosmochim. Acta. 330, 148–164.
Goswami, S., Upadhyay, P.K., Saravanan, B., Natarajan, V., Verma, M.B., 2019. Two types of uranium mineralization in Gulcheru quartzite: Fracture-controlled in Ambakapalle area and litho-controlled in Tummalapalle area, Cuddapah Basin, Andhra Pradesh, India. China Geol. 2 (2), 142–156.
Götz, C., Geipel, G., Bernhard, G., 2011. The influence of the temperature on the carbonate complexation of uranium (VI): a spectroscopic study. J. Radioanal. Nucl. Chem. 287 (3), 961–969.
Guo, F., Li, Z., Deng, T., Qu, M., Zhou, W., Huang, Q., Shang, P., Zhang, C., Yan, Z., 2020. Key factors controlling volcanic-related uranium mineralization in the Xiangshan Basin, Jiangxi Province, South China: a review. Ore Geol. Rev. 122, 1–15.
Helgeson, H.C., Garrels, R.M., MacKenzie, F.T., 1969. Evaluation of irreversible reactions in geochemical processes involving minerals and aqueous solutions—II. Applications. 33 (4), 455–481.
Hemingway, B.S., Seal II, R.R., Chou, I.-M., 2002. Thermodynamic Data for Modeling Acid Mine Drainage Problems: Compilation and Estimation of Data for Selected Soluble Iron-Sulfate Minerals, 2331-1258.
Hoeve, J., Sibbald, T.I.I., 1978. On the genesis of Rabbit Lake and other unconformity-type uranium deposits in northern Saskatchewan, Canada. Econ. Geol. 73 (8), 1450–1473.
Hu, R.-Z., Bi, X.-W., Zhou, M.-F., Peng, J.-T., Su, W.-C., Liu, S., Qi, H.-W., 2008. Uranium metallogenesis in South China and its relationship to crustal extension during the cretaceous to Tertiary. Econ. Geol. 103 (3), 583–598.
Hu, R.-Z., Burnard, P., Bi, X.-W., Zhou, M.-F., Peng, J.-T., Su, W.-C., Zhao, J.-H., 2009. Mantle-derived gaseous components in ore-forming fluids of the Xiangshan uranium deposit, Jiangxi province, China: evidence from He, Ar and C isotopes. Chem. Geol. 266 (1–2), 86–95.
IAEA (International Atomic Energy Agency), 2018. Geological Classification of Uranium Deposits and Description of Selected Examples, IAEA-TECDOC-1842, p. 417.
Ilton, E.S., Haiduc, A., Moses, C.O., Heald, S.M., Elbert, D.C., Veblen, D.R., 2004. Heterogeneous reduction of uranyl by micas: Crystal chemical and solution controls. Geochim. Cosmochim. Acta 68 (11), 2417–2435.
Ilton, E.S., Haiduc, A., Cahill, C.L., Felmy, A.R., 2005. Mica surfaces stabilize pentavalent uranium. Inorg. Chem. 44 (9), 2986–2988.
Kalintsev, A., Migdisov, A., Alcorn, C., Baker, J., Brugger, J., Mayanovic, R.A., Akram, N., Guo, X., Xu, H., Boukhalfa, H., Caporuscio, F.A., Viswanathan, H., Jove-Colon, C., Wang, Y., Matteo, E., Roback, R., 2021. Uranium carbonate complexes demonstrate drastic decrease in stability at elevated temperatures. Communicat. Chem. 4, 1–8.
Komninou, A., Sverjensky, D., 1996. Geochemical modeling of the formation of an unconformity-type uranium deposit. Econ. Geol. 91 (3), 590–606.
Kotzer, T., Kyser, T., 1995. Petrogenesis of the Proterozoic Athabasca Basin, northern Saskatchewan, Canada, and its relation to diagenesis, hydrothermal uranium mineralization and paleohydrogeology. Chem. Geol. 120 (1–2), 45–89.
Langmuir, D., 1978. Uranium solution-mineral equilibria at low temperatures with applications to sedimentary ore deposits. Geochim. Cosmochim. Acta 42 (6, Part A), 547–569.
Lasaga, A.C., 2014. Rate Laws of Chemical Reactions, Kinetic Theory in the Earth Sciences. Princeton University Press, pp. 1–151.
Liang, R., Chi, G., Ashton, K., Blamey, N., Fayek, M., 2017. Fluid compositions and P-T conditions of vein-type uranium mineralization in the Beaverlodge uranium district, northern Saskatchewan, Canada. Ore Geol. Rev. 80, 460–483.
Liger, E., Charlet, L., Van Cappellen, P., 1999. Surface catalysis of uranium(VI) reduction by iron(II). Geochim. Cosmochim. Acta 63 (19), 2939–2955.
Liu, W., Etschmann, B., Brugger, J., Spiccia, L., Foran, G., McInnes, B., 2006. UV–Vis spectrophotometric and XAFS studies of ferric chloride complexes in hyper-saline LiCl solutions at 25–90 C. Chem. Geol. 231 (4), 326–349.
Liu, W., Etschmann, B., Foran, G., Shelley, M., Brugger, J., 2007. Deriving formation constants for aqueous metal complexes from XANES spectra: Zn2+ and Fe2+ chloride complexes in hypersaline solutions. Am. Mineral. 92 (5–6), 761–770.
Marshall, W.L., Franck, E.U., 1981. Ion product of water substance, 0–1000 C, 1–10,000 bars. J. Phys. Chem. Ref. Data 10, 295–304.
Martz, P., Mercadier, J., Cathelineau, M., Boiron, M.-C., Quirt, D., Doney, A., Gerbeaud, O., De Wally, E., Ledru, P., 2019. Formation of U-rich mineralizing fluids through basinal brine migration within basement-hosted shear zones: A large-scale study of the fluid chemistry around the unconformity-related Cigar Lake U deposit (Saskatchewan, Canada). Chem. Geol. 508, 116–143.
Mercury, L., Vieillard, P., Tardy, Y., 2001. Thermodynamics of ice polymorphs and 'ice-like'water in hydrates and hydroxides. Appl. Geochem. 16 (2), 161–181.
Mernagh, T.P., Heinrich, C.A., Leckie, J.F., Carville, D.P., Gilbert, D.J., Valenta, R.K., Wyborn, L.A.I., 1994. Chemistry of low-temperature hydrothermal gold, platinum, and palladium (+ or - uranium) mineralization at Coronation Hill, Northern Territory, Australia. Econ. Geol. 89 (5), 1053–1073.
Migdisov, A., Guo, X., Nisbet, H., Xu, H., Williams-Jones, A.E., 2019. Fractionation of REE, U, and Th in natural ore-forming hydrothermal systems: Thermodynamic modeling. J. Chem. Thermodyn. 128, 305–319.
Ng, R., Alexandre, P., Kyser, K., 2013a. Mineralogical and Geochemical Evolution of the Unconformity-Related McArthur River Zone 4 Orebody in the Athabasca Basin, Canada: Implications of a Silicified Zone*. Econ. Geol. 108 (7), 1657–1689.
Ng, R., Alexandre, P., Kyser, K., Cloutier, J., Abdu, Y.A., Hawthorne, F.C., 2013b. Oxidation state of iron in alteration minerals associated with sandstone-hosted unconformity-related uranium deposits and apparently barren alteration systems in the Athabasca Basin, Canada: Implications for exploration. J. Geochem. Explor. 130, 22–43.
Pan, Y., Li, D., Feng, R., Wiens, E., Chen, N., Chernikov, R., Götze, J., Lin, J., 2021. Uranyl binding mechanism in microcrystalline silicas: A potential missing link for uranium mineralization by direct uranyl co-precipitation and environmental implications. Geochim. Cosmochim. Acta 292, 518–531.
Rabiei, M., Chi, G., Potter, E., Tschirhart, V., MacKay, C., Frostad, S., McElroy, R., Ashley, R., McEwan, B., 2021. Fluid evolution along the Patterson Lake corridor in the southwestern Athabasca Basin: constraints from fluid inclusions and implications for unconformity-related uranium mineralization. Geochem.: Explorat., Environ., Anal. 21 (3).
Richard, A., Pettke, T., Cathelineau, M., Boiron, M.C., Mercadier, J., Cuney, M., Derome, D., 2010. Brine–rock interaction in the Athabasca basement (McArthur River U deposit, Canada): consequences for fluid chemistry and uranium uptake. Terra Nova 22 (4), 303–308.
Richard, A., Rozsypal, C., Mercadier, J., Banks, D.A., Cuney, M., Boiron, M.-C., Cathelineau, M., 2012. Giant uranium deposits formed from exceptionally uranium-rich acidic brines. Nat. Geosci. 5 (2), 142.
Richard, A., Boulvais, P., Mercadier, J., Boiron, M.-C., Cathelineau, M., Cuney, M., France-Lanord, C., 2013. From evaporated seawater to uranium-mineralizing brines: Isotopic and trace element study of quartz–dolomite veins in the Athabasca system. Geochim. Cosmochim. Acta 113, 38–59.
Richard, A., Cathelineau, M., Boiron, M.-C., Mercadier, J., Banks, D.A., Cuney, M., 2016. Metal-rich fluid inclusions provide new insights into unconformity-related U deposits (Athabasca Basin and Basement, Canada). Mineral. Deposita 51 (2), 249–270.
Robie, R.A., Hemingway, B.S., 1995. Thermodynamic Properties of Minerals and Related Substances at 298.15 K and 1 Bar (105 Pascals) Pressure and at Higher Temperatures, 2131. US Government Printing Office.
Romberger, S.B., 1984. Transport and Deposition of Uranium in Hydrothermal Systems at Temperatures up to 300 C: Geological Implications, Uranium Geochemistry, Mineralogy, Geology, Exploration and Resources. Springer, pp. 12–17.
Rozsypal, C., Chinh, N.-T., Cuney, M., 2009. Experimental study and modelling of the U (VI)-NaCl-H 2 O ternary system with respect to pH and NaCl concentration at T= 155 degrees C and Psat. Géochim. Géol. l'Uranium 18.
Scholten, L., Schmidt, C., Lecumberri-Sanchez, P., Newville, M., Lanzirotti, A., Sirbescu, M.-L.C., Steele-MacInnis, M., 2019. Solubility and speciation of iron in hydrothermal fluids. Geochim. Cosmochim. Acta 252, 126–143.
Shock, E.L., Sassani, D.C., Willis, M., Sverjensky, D.A., 1997. Inorganic species in geologic fluids: correlations among standard molal thermodynamic properties of aqueous ions and hydroxide complexes. Geochim. Cosmochim. Acta 61 (5), 907–950.
Shvarov, Y.V., Bastrakov, E.N., 1999. HCh: A Software Package for Geochemical Equilibrium Modelling. User's Guide.
Soderholm, L., Skanthakumar, S., Wilson, R.E., 2011. Structural correspondence between uranyl chloride complexes in solution and their stability constants. J. Phys. Chem. A 115 (19), 4959–4967.
Song, H., Chi, G., Wang, K., Li, Z., Bethune, K., Potter, E., Liu, Y., 2022. The role of graphite in the formation of unconformity-related uranium deposits of the Athabasca Basin, Canada: a case study of Raman spectroscopy of graphite from the world-class Phoenix uranium deposit. Am. Mineral. 107 (11), 2128–2142.
Stefánsson, A., 2007. Iron (III) hydrolysis and solubility at 25 C. Environ. Sci. Technol. 41 (17), 6117–6123.
Stefánsson, A., Lemke, K.H., Seward, T.M., 2019. Iron (III) chloride complexation in hydrothermal solutions: A combined spectrophotometric and density functional theory study. Chem. Geol. 524, 77–87.
Sverjensky, D., Shock, E., Helgeson, H.J., 1997. Prediction of the thermodynamic properties of aqueous metal complexes to 1000 C and 5 kb, 61 (7), 1359–1412.
Testemale, D., Brugger, J., Liu, W., Etschmann, B., Hazemann, J.-L., 2009. In-situ X-ray absorption study of iron (II) speciation in brines up to supercritical conditions. Chem. Geol. 264 (1–4), 295–310.
Timofeev, A., Migdisov, A.A., Williamsjones, A.E., Roback, R., Nelson, A.T., Xu, H., 2018. Uranium transport in acidic brines under reducing conditions. Nat. Commun. 9 (1), 1–7.
Villa-Alfageme, M., Hurtado, S., El Mrabet, S., Pazos, M.C., Castro, M.A., Alba, M.D., 2015. Uranium immobilization by FEBEX bentonite and steel barriers in hydrothermal conditions. Chem. Eng. J. 269, 279–287.
Volzhin, D.D., Korolev, K.G., 1982. Characteristics of epigenetic uranium mineralization in jasper-quartzites. Int. Geol. Rev. 24 (6), 694–700.
Wang, K., Chi, G., Bethune, K.M., Li, Z., Blamey, N., Card, C., Potter, E.G., Liu, Y., 2018. Fluid PTX characteristics and evidence for boiling in the formation of the Phoenix uranium deposit (Athabasca Basin, Canada): Implications for unconformity-related uranium mineralization mechanisms. Ore Geol. Rev. 101, 122–142.
Wang, Y., Chi, G., Li, Z., Bosman, S., 2021. Large-scale thermal convection in sedimentary basins revealed by coupled quartz cementation-dissolution distribution pattern and reactive transport modeling – a case study of the Proterozoic Athabasca Basin (Canada). Earth Planet. Sci. Lett. 574, 1–9.
Wersin, P., Hochella, M.F., Persson, P., Redden, G., Leckie, J.O., Harris, D.W., 1994. Interaction between aqueous uranium (VI) and sulfide minerals: Spectroscopic evidence for sorption and reduction. Geochim. Cosmochim. Acta 58 (13), 2829–2843.
Xing, Y., Mei, Y., Etschmann, B., Liu, W., Brugger, J., 2018. Uranium transport in F-Cl-bearing fluids and hydrothermal upgrading of U-Cu ores in IOCG deposits. Geofluids 2018, 1–22.
Xing, Y., Etschmann, B., Liu, W., Mei, Y., Shvarov, Y., Testemale, D., Tomkins, A., Brugger, J., 2019. The role of fluorine in hydrothermal mobilization and

transportation of Fe, U and REE and the formation of IOCG deposits. Chem. Geol. 504, 158–176.
Yu, Z., Ling, H., Mavrogenes, J., Chen, P., Chen, W., 2019. Metallogeny of the Zoujiashan uranium deposit in the Mesozoic Xiangshan volcanic-intrusive complex, Southeast China: insights from chemical compositions of hydrothermal apatite and metal elements of individual fluid inclusions. Ore Geol. Rev. 113, 1–22.
Zhang, L., Chen, Z., Wang, F., White, N.C., Zhou, T., 2021. Release of uranium from uraninite in granites through alteration: implications for the source of granite-related uranium ores. Econ. Geol. 116 (5), 1115–1139.
Zhao, R., Pan, P., 2001. A spectrophotometric study of Fe (II)-chloride complexes in aqueous solutions from 10 to 100 C. Can. J. Chem. 79 (2), 131–144.